Original Article

Addition of hematite as a sintering aid in alumina: effect of concentration on physical, microstructural and mechanical properties

Pedro Henrique Poubel Mendonça da Silveira [1,2*] ⓘ
Amal Elzubair Eltom [2] ⓘ
Jheison Lopes dos Santos [3] ⓘ
Geovana Carla Girondi Delaqua [4] ⓘ
Carlos Maurício Fontes Vieira [4] ⓘ
Paulo Roberto Rodrigues de Jesus [2]
Marcelo Henrique Prado da Silva [2] ⓘ
Alaelson Vieira Gomes [2] ⓘ

Abstract

Hematite (Fe_2O_3), or ferric oxide, is a ceramic oxide that, despite being recognized in the field of science and materials engineering, finds limited use as a sintering additive. Therefore, the purpose of this study was to explore the incorporation of hematite as a sintering additive in alumina (Al_2O_3), employing conventional sintering at 1400 °C. Seven compositions were processed, with Fe_2O_3 content varying from 0 to 8 wt.%. The samples underwent conventional ceramic processing steps (homogenization, drying, deagglomeration, sieving, and cold uniaxial pressing), followed by sintering at 1400 °C. The physical and mechanical properties of the produced samples were assessed through dilatometry, density measurement using the Archimedes' method, scanning electron microscopy with energy-dispersive spectroscopy (SEM/EDS), and flexural and compression tests. The results revealed that the addition of 4 and 6 wt.% of Fe_2O_3 resulted in reduced shrinkage of the ceramics, leading to low densification, highly porous surfaces, and diminished flexural strength. On the other hand, lower additions (0.5, 1, and 2 wt.%) of Fe_2O_3 improved the sintering of Al_2O_3, yielding samples with increased flexural and compressive strength, linear shrinkage, and densification.

Keywords: Alumina; Hematite; Flexural resistance; Sintering.

1 Introduction

Ceramics based on alumina (Al_2O_3) have been the subject of numerous studies in structural applications, owing to their remarkable properties such as dimensional stability, high-temperature resistance, and high hardness [1]. Al_2O_3 has characteristics similar to other polycrystalline ceramics, such as moderate tensile and bending resistance, and brittle fracture behavior, which is the main disadvantage of the mechanical properties of alumina. Al_2O_3 is an ionic-covalent solid that does not yield under load like metals and alloys. The strong chemical bonds in Al_2O_3 are reflected in its characteristics, such as low electrical and thermal conductivity, the high melting point that makes it practically impossible to shape alumina by casting, and the high hardness that characterizes this material and makes its machining complex and costly [2]. The brittleness of Al_2O_3 is another property that concerns engineers when designing components using this material. In metals, crack energy is dissipated by deformation at the crack tip, while alumina components can fail without any previous plastic deformation at the location of high tensile stresses, such as surface defects, notches, internal flaws, or in the occurrence of thermal shocks [3]. With the advancement of materials science and engineering, the use of new techniques and/or materials is employed in ceramics so that their properties can be improved, and their disadvantages reduced, making these materials applicable, either as structural material or as functional material [4,5].

The addition of sintering additives with a low melting point creates a layer of a liquid phase, making it possible to sinter and bond ceramic particles at lower temperatures [6]. The liquid phase formed by the additives "wets" the ceramic particles, and flows between them, causing the rearrangement of the particles, increasing the densification of the material. The surface tension of the liquid phase assists in the densification and removal of ceramic pores [7,8].

Metal oxides such as CaO, MgO, BaO, Nb_2O_5, Y_2O_3, SiO_2, ZrO_2 among others are commonly used for liquid phase formation in the sintering process [9-18]. In addition, ternary eutectic compositions are also used to produce liquid phases with a low melting point. Since most ternary phase diagrams have more than one eutectic point, the selection of the appropriate eutectic composition depends on the desired properties of the ceramic [19].

The Al_2O_3-Fe_2O_3 compound is a mixed oxide system, commonly used as a sorbent and catalyst. This compound is the subject of several investigations regarding its physicochemical properties [20-23]. Alumina and hematite have applications in catalysis and adsorption [22,24]. The main characteristics of alumina powders are surface acidity, mechanical strength, high surface area, and stability against sintering, insulating and diamagnetic properties [25]. On the other hand, hematite powders present as main characteristics the redox behavior, medium to low surface area, easy sintering, semiconductor, and antiferromagnetic properties derived from iron [26]. In theory, the chemical mixing of Fe_2O_3 with Al_2O_3 could be beneficial, enabling the production of oxidation catalysts with improved stability or mechanically and thermally stable powders with redox functionality. Furthermore, the treatment of two oxides at high temperatures produces new crystal structures with interesting properties, especially in heterogeneous catalysis, different from the properties of the initial oxides [27].

Considering the Fe_2O_3-Al_2O_3 system, some studies have been crucial for understanding phase formation from this compound. Muan and Gee [27] and Muan [28] verified phase formation from this compound between 1085 and 1725 °C with oxygen pressure (PO_2) variation, where the formation of $FeAlO_3$ was verified at pressures higher than 0.03 atm. The $FeAlO_3$ phase was also found to be unstable, to decompose into hematite and corundum at temperatures below 1318 °C, where the decomposition temperature remains unchanged with respect to PO_2.

The stability of $FeAlO_3$ increases with increasing pressure, where the stabilization temperature of $FeAlO_3$ ranges from 1318 to 1410 °C in air, changing to 1318-1495 °C at PO_2 = 1 atm.

From Muan's initial studies, other studies were published in order to extend the limits of knowledge on this subject: Dayal et al. [29] performed a crystal structure analysis, where they showed that $FeAlO_3$ has an orthorhombic structure with a Pc21n space group. Feenstra et al. [30] disclosed the synthesis of the orthorhombic $(Fe_{0.53}Al0.47)_2O_3$ phase coexisting with the corundum $(Al_{0.88}Fe_{0.12})_2O_3$ at 1300 °C, a temperature lower than that required for the stabilization of $FeAlO_3$ (1318 °C). Dreval et al. [31] presented ternary phase diagrams calculated in the Al_2O_3-Fe_2O_3-FeO system based on experimental data for relevant phases. The results obtained by the authors are similar to those of Muan [28]. Majzlan et al. [32] determined the enthalpy of $FeAlO_3$ formation from hematite and corundum and estimated the entropy of formation, indicating that $FeAlO_3$ is unstable under high-temperature P-T metamorphic conditions. The Al_2O_3-Fe_2O_3 system has interesting characteristics, however, concerning the properties of alumina when utilizing hematite as a sintering aid, only the study by Wang et al. [33] addresses aspects such as ceramic densification with varying Fe_2O_3 compositions, in addition to flexural strength.

This work aims to expand the knowledge about the properties of the Al_2O_3-Fe_2O_3 compound by analysing its behaviour during sintering, morphology, and mechanical properties, especially through flexural and compressive testing.

2 Materials and methods

2.1 Materials

The materials used in the fabrication of ceramic bodies are: α-Al_2O_3 (ρ = 3.96 g/cm³; Alcoa P-913, Brazil), with a particle size of 1μm, glycine (Sigma Aldrich), and iron nitrate (Neon Química, Brazil), employed for the preparation of hematite (Fe_2O_3) powders (ρ = 5.26 g/cm³). Polyethylene glycol (PEG) (Isofar, Brazil) was added to provide mechanical strength to the green bodies. The theoretical density of the samples was determined using the Rule of Mixtures, excluding PEG which is eliminated during sintering. Table 1 presents the theoretical density (TD) values and nomenclature of each sample.

Table 1. Composition, nomenclature and theoretical density of sample groups of this paper

SAMPLE	COMPOSITION	DENSITY (g/cm³)
AL	100 wt.% Al_2O_3	3.960
ALFE05	99.5 wt.% Al_2O_3 – 0.5 wt.% Fe_2O_3	3.966
ALFE10	99 wt.% Al_2O_3 – 1 wt.% Fe_2O_3	3.973
ALFE20	98 wt.% Al_2O_3 – 2 wt.% Fe_2O_3	3.986
ALFE40	96 wt.% Al_2O_3 – 4 wt.% Fe_2O_3	4.012
ALFE60	94 wt.% Al_2O_3 – 6 wt.% Fe_2O_3	4.038
ALFE80	92 wt.% Al_2O_3 – 8 wt.% Fe_2O_3	4.064

2.2 Fe$_2$O$_3$ powder synthesis

The Fe$_2$O$_3$ powders were obtained through the spontaneous combustion synthesis method. In this process, ferric nitrate [Fe(NO$_3$)$_3$·9H$_2$O] was used as the oxidizer, and glycine [NH$_2$CH$_2$COOH] as the fuel. This method was similar to the one performed in the study by Cao et al. [34]. To prepare the powders, Fe(NO$_3$)$_3$·9H$_2$O and NH$_2$CH$_2$COOH were dissolved in 150 mL of distilled water and the solution was stirred to achieve a homogeneous mixture. Subsequently, the mixture was poured into a 500 mL beaker and heated to 100 °C.

During the heating process, the water in the solution evaporated, transforming the mixture into a gelatinous mass. After a few minutes of heating, the mixture expanded, releasing a significant amount of gases. This was followed by a non-explosive exothermic reaction, resulting in spontaneous combustion. After the burn, a foam composed of iron oxide was obtained, which was crushed to produce the Fe$_2$O$_3$ powders used as sintering additives.

2.3 Ceramic processing

To obtain the desired materials, Al$_2$O$_3$, Fe$_2$O$_3$, and PEG were homogenized in a ball mill for 8h, using distilled water in a 1:1 ratio to facilitate the mixture. After this process, the powders were dried for 48h at a temperature of 120 °C, manually deagglomerated, and sieved through a 60-mesh screen. Using these materials, discs with a diameter of 15 mm and a mass of 0.5 g were produced through cold uniaxial pressing with a load of 30 MPa. Sintering was conducted in a JUNG furnace, without the application of pressure, with a maximum temperature of 1400 °C, followed by inertial cooling. The heating ramp utilized is illustrated in Figure 1.

2.3 Characterization

2.3.1 Dilatometric analysis

Dilatometric analyses were conducted using the Netzsch DIL402 PC dilatometer in the Laboratory of Advanced Materials (LAMAV) at the Universidade Estadual do Norte Fluminense (UENF). The thermal cycle for this analysis commenced at room temperature, where the samples were heated at a rate of 5 °C/min up to 1400 °C, holding at this temperature for 1 hour, followed by cooling at a rate of 10 °C/min. The samples used in the dilatometry test have a diameter of 12mm and a length of 6mm. The samples were heated in an Al$_2$O$_3$ crucible, which can withstand temperatures up to 1600 °C. To rectify the obtained results and eliminate any thermal expansion curves that might emerge due to dilatometer variations, the thermal expansion constant (α) value is derived using Equation 1. This value serves as a basis for determining the technological shrinkage (ε_{tech}), as presented in Equation 2.

Technological shrinkage employs the thermal expansion constant value to exclude expansion readings during the analysis, thereby representing only the accurate material shrinkage value [35].

$$\alpha = \frac{\varepsilon_{amb} - \varepsilon_{máx}}{(T_{amb} - T_{máx}) \cdot 100} \tag{1}$$

Where: ε_{amb} represents the material shrinkage after cooling; ε_{max} signifies the material shrinkage at the maximum temperature; T_{amb} stands for the final temperature after cooling, and T_{max} denotes the maximum temperature of the test.

$$\varepsilon_{tech}(t,T) = \varepsilon(t,T) - \alpha \cdot 100 \cdot (T - T_{amb}) \tag{2}$$

Where: $\varepsilon(t,T)$ represents the shrinkage at a specific point; t stands for the time at which the formula was applied, and T denotes the temperature at that particular point.

2.3.2 Green density calculation

Prior to sintering, the density of the material in its green form was determined by measuring the mass and calculating the volume of the green bodies using Equation 3. Furthermore, green state densification (Equation 4) was calculated as the percentage difference between the measured density and the theoretical density obtained through the Rule of Mixtures.

$$\rho_g = \frac{m}{v} \tag{3}$$

$$d_g = \left(\frac{\rho verde}{\rho}\right) \cdot 100\% \tag{4}$$

Where: ρ_g - density of the green body (g/cm³); m - mass of the body (g); v - volume of the body (cm³); ρ - theoretical density (g/cm³); d_g - densification of the green body (%).
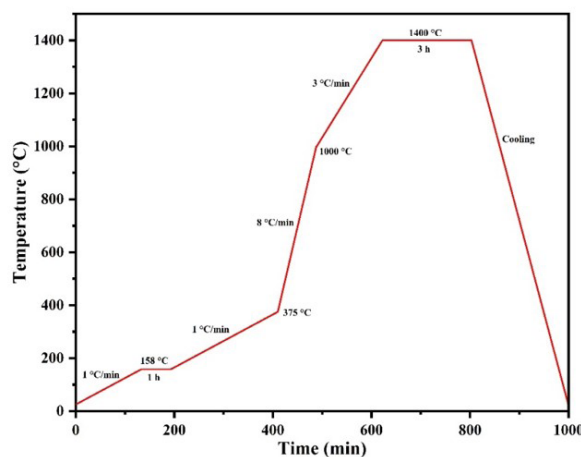

Figure 1. Sintering ramp adopted in this study.

2.3.3 Density and linear shrinkage of sintered samples

To calculate the densification of the sintered bodies, the method described in NBR 16667:2017 [36], based on the Archimedes technique, was employed. Using the immersed mass (m_i), wet mass (m_w), and dry mass (m_d) data, it was possible to determine the apparent density through Equation 5. With this result, the densification of the ceramic body was then calculated by the difference between the apparent density and the relative density of the sintered body (Equation 6).

$$\rho ap = \frac{md}{mw - mi} \cdot \rho_{water} \quad (5)$$

$$Densif\ (\%)\ = \frac{\rho ap}{\rho teo} \cdot 100\% \quad (6)$$

To calculate the linear shrinkage (L_S) of the sintered bodies, the difference between the diameter of the green body (D_{GB}) and the sintered body (D_{SB}) was employed, as shown in Equation 7.

$$L_S = \frac{D_{GB} - D_{SB}}{D_{SB}} \cdot 100\% \quad (7)$$

2.3.4 Scanning Electron Microscopy (SEM)

The sintered samples were morphologically analyzed using the QUANTA FEG 250 microscope, manufactured by FEI. The samples underwent ceramic preparation, being embedded and then ground successively with #220, #400, #600, #1200, and #2000 grit sandpapers, followed by polishing with 6µm diamond paste. Subsequent to preparation, the samples were coated with gold utilizing a Leica ACE600 high-vacuum coating chamber. SEM analysis was carried out under the following parameters: electron beam power of 20kV, working distance ranging between 10.5 to 13 mm, spot size of 5, and image magnification at 20,000x, utilizing the secondary electron detector. For EDX analysis and compositional mapping, a detector from the manufacturer Bruker was employed, coupled to the microscope column.

2.3.5 Flexural tests

Flexural strength testing of the studied materials was performed on ceramic discs with a diameter of 14 ± 2 mm and a thickness of 1.2 ± 0.2 mm, following the ABNT NBR ISO 6872:2016 Standard [37]. Six samples were tested for each group, positioned atop three metallic spheres, and subjected to a rate of 0.5 mm/min until fracture occurred. The flexural strength was automatically calculated by the software based on the data collected by the equipment. The test was conducted at the Mechanical Testing Laboratory of IME, using a DL-1000 EMIC machine.

2.3.6 Compressive tests

The compressive test of the samples was carried out on a DL-1000 EMIC machine at a testing speed of 0.5 mm/min. For each group, three samples were used, prepared in a cylindrical shape following the method described by Awaji, Watanabe, and Nagano for compressive testing [38]. The samples used have a diameter of 12.5 mm and a thickness of 5 mm.

3 Results and discussion

3.1 Dilatometric analysis

In Figure 2 and Table 2, the results of dilatometry for the studied samples are shown. The inclusion of Fe_2O_3 as a sintering aid in Al_2O_3 resulted in significant changes in behavior during the sintering process. The addition of 0.5 and 1 wt.% of Fe_2O_3, represented by samples ALFE05 and ALFE10, respectively, did not influence the onset retraction temperature (indicated as T_1 in the table). The final retraction temperatures (T_2) showed no variation in the compound samples, while the maximum retraction temperature (T_3) of samples ALFE05 and ALFE10 exhibited a reduction. Compared to the AL group, sample ALFE05 showed a lower retraction, with a value of $\epsilon = 9.04\%$, while sample ALFE10 presented a value of $\epsilon = 11.59\%$.
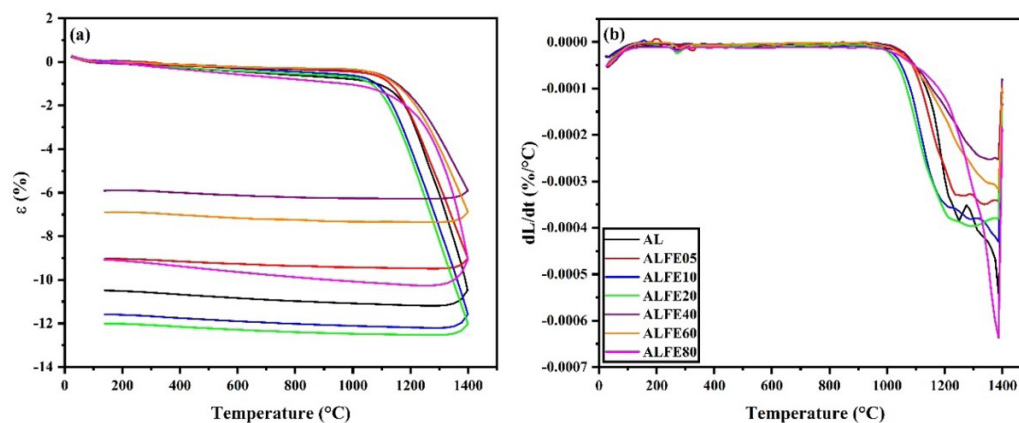
Figure 2. Dilatometric Curves: (a) Shrinkage Curves; (b) Shrinkage Rate Curves.

The addition of 2 wt.% Fe_2O_3 in the ALFE20 sample resulted in a reduction of T1, with shrinkage starting at 1010 °C, and an increase in T_3, reaching 1286 °C. The samples containing 4 and 6 wt.% of Fe_2O_3 (ALFE40 and ALFE60) exhibited a delayed onset of shrinkage compared to other compound samples, with T_1 values of 1060 and 1047 °C, respectively, and an increase in T_2. The higher T_1 values indicate that higher temperatures, or in other words, higher activation energy values, are necessary for the shrinkage to begin [39]. Depending on the sintering temperature and the time employed, good densification of the material may not occur. If the sintering temperature is low, remaining below the maximum shrinkage point (T_3), and the sintering time is short, proper grain rearrangement and growth may not occur, thus compromising the final densification of the ceramic [8]. The shrinkage values obtained for these samples were the lowest among all groups, with ϵ equal to 5.90% and 6.89%, respectively. The ALFE80 sample present a T_1 temperature similar to the ALFE60 sample. Its T_2 was recorded at 1386 °C, close to the maximum test temperature, while it was not possible to record T_2, as it is above 1400 °C. Its shrinkage was similar to that of group ALFE05, with a value of 9.05%.

When observing the temperatures T_1, T_2, and T_3, it is noticeable that there is a tendency for the ϵ value of the samples to increase as the temperatures T_1 and T_3 decrease, due to the greater activation energy required to initiate the shrinkage during sintering. This is evidenced by the value of alpha. This trend is observed in the ALFE10 and ALFE20 samples, which showed the highest ϵ values, with ALFE10 exhibiting a lower T_3 value and the ALFE20 sample presenting a lower temperature at T_1. However, the ALFE80 sample exhibited an abnormal behavior, with an ϵ value similar to that of the ALFE05 sample, but with much higher T_1 and T_3 values. Low ϵ values can lead to materials with low densification and high porosity.

Residual porosity in ceramics leads to a decrease in the mechanical strength of the final product. As a result, porous ceramics generally exhibit lower mechanical resistance when compared to dense ceramics. Consequently, their applications are distinct and cannot be used as structural materials [40].

From the calculation of the thermal expansion constant (α), as shown in Equation 1, it was observed that the value of α is inversely proportional to the material shrinkage.

It can be observed that as the shrinkage value increases, α decreases. This observation is supported by the work of Zygmuntowicz et al. [41], where the authors studied the sintering behavior of the Al_2O_3-Ni compound and, through dilatometry analysis, found that the α of samples with a higher Ni content increased due to lower shrinkage values of the compound compared to pure Al_2O_3. Some examples in the literature demonstrate the influence of sintering additives on the shrinkage curves of alumina. García et al. [42] processed Al_2O_3 - Nb compounds in fractions of 10, 30, and 50 vol.%. Through dilatometry tests, the authors observed that the onset of shrinkage began at 850 °C due to the addition of Nb. However, to achieve a 12% shrinkage value, it was necessary to add 50 vol.% of Nb. Jesus et al. [43] reports the production of functional gradient ceramics (FGM) using the spark plasma sintering (SPS) method, employing a compound of Al_2O_3 - Nb_2O_5 - LiF - ZrO_2. In order to investigate which compositions would present similar shrinkage curves for the formation of FGM layers, dilatometry technique was used. The addition of ZrO_2 to Al_2O_3 resulted in an ϵ value of 15%, while compositions with different levels of LiF added to the Al_2O_3 - Nb_2O_5 compound maintained lower ϵ values, close to 13%. The significant difference in ϵ values resulted in a large amount of residual stress, leading to the formation of cracks during the processing of FGMs by SPS, as well as reducing the mechanical strength and densification of the material.

3.2 Density and linear shrinkage of samples

Figure 3 shows the density results of the green bodies, density of sintered samples, and linear shrinkage are illustrated.

The results presented in Figure 3(a) indicate that the addition of Fe_2O_3 influenced the densification of the green bodies during compaction. A slight increase in the density of the ALFE05, ALFE10, and ALFE20 bodies was observed compared to pure alumina after the addition of 0.5, 1, and 2 wt.% of Fe_2O_3. The AL group exhibited a relative green density of 57.79 ± 2.40% of the theoretical density, while the samples from the ALFE05, ALFE10, and ALFE20 groups exhibited relative green densities of 60.89 ± 1.92%, 61.14 ± 2.53%, and 59.00 ± 1.37%, respectively.

Table 2. Shrinkage temperatures, thermal expansion coefficient, and shrinkage values obtained in the dilatometric analysis

SAMPLE	T_1 (°C)	T_2 (°C)	T_3 (°C)	α (10^{-6} K^{-1})	ϵ (%)
AL	1035	1387	1249	6.51	10.48
ALFE05	1035	1386	1235	6.61	9.04
ALFE10	1035	1386	1210	6.42	11.59
ALFE20	1010	1382	1286	6.39	12.03
ALFE40	1060	1386	1348	6.84	5.90
ALFE60	1047	1386	1336	6.77	6.89
ALFE80	1047	-	1386	6.61	9.05

On the other hand, the addition of higher percentages of Fe_2O_3 resulted in a reduction in the average density of the green bodies. The samples with 4 and 6 wt.% Fe_2O_3 additions (ALFE40 and ALFE60) exhibited relative densities of $52.78 \pm 2.20\%$ and $55.87 \pm 3.87\%$, respectively. The sample with 8 wt.% of Fe_2O_3 (ALFE80) presented an average density value of $53.29 \pm 3.64\%$. The high Fe_2O_3 content in the samples may have hindered homogenization, causing the reduction in density of the ALFE40, ALFE60, and ALFE80 groups.

Regarding densification after sintering, as illustrated in Figure 3(b), the AL group exhibited a relative densification of $82.99 \pm 0.82\%$. Adding 0.5 wt.% Fe_2O_3 resulted in a slight reduction in the densification of the ALFE05 group, which reached $79.06 \pm 1.89\%$. On the other hand, the addition of 1 and 2 wt.% of Fe_2O_3 led to a slight increase in the relative density of the ALFE10 and ALFE20 groups, which had values of $83.64 \pm 0.75\%$ and $85.69 \pm 1.16\%$, respectively. The addition of Fe_2O_3 at concentrations of 4 and 6 wt.% resulted in a significant reduction in the densification of the ALFE40 and ALFE60 groups, which exhibited values of $66.96 \pm 1.83\%$ and $62.69 \pm 0.99\%$ of TD, respectively. The ALFE80 group exhibited a relative densification of $88.24 \pm 2.91\%$, the highest value among all compositions.

The results of linear shrinkage of the sintered samples shown in Figure 3(b) corroborate the results of the dilatometric analysis. The addition of Fe_2O_3 up to 2 wt.% causes an increase in shrinkage, with a consequent increase in densification, except for the ALFE05 sample, which showed a reduction in the ε value in dilatometry compared to AL. In the calculation of linear shrinkage, the AL group exhibited a shrinkage of $11.24 \pm 0.23\%$, while ALFE05 exhibited a shrinkage of $13.56 \pm 1.31\%$. The ALFE10 and ALFE20 samples exhibited shrinkage of $16.28 \pm 0.39\%$ and $16.00 \pm 0.37\%$, respectively. The ALFE40 and ALFE60 groups,

which exhibited low densification values, showed linear shrinkage of $5.28 \pm 0.77\%$ and $3.89 \pm 0.50\%$, respectively. The ALFE80 group exhibited a linear shrinkage value of $12.89 \pm 0.27\%$. The sample presented an unexpected result, given that the shrinkage value from the dilatometry test of the sample was similar to that of the ALFE05 sample, which exhibited lower densification after sintering. The difference in the shrinkage values obtained with dilatometry and calculated after sintering is due to the difference in the heating rates of the test and the sintering ramp, as well as the dwell time at the sintering temperature. The longer dwell time in sintering allowed for grain growth in the sample, increasing densification.

3.3 Scanning Electron Microscopy (SEM)

In Figure 4, the surface micrographs of the samples captured by SEM with a magnification of 5000x are illustrated. The presence of Fe_2O_3 in Al_2O_3 influenced densification, as shown in the dilatometry and density results, but the morphology changed with an increasing amount of sintering additive. Pure alumina (group AL), shown in Figure 4(a), exhibits a microstructure characterized by a series of small interconnected pores, indicated by yellow arrows in the figure, as well as isolated and loosely cohesive grains. These characteristics are attributed to low densification, confirmed by the obtained densification results and Rahaman's study (2017), reporting that the initial stage of sintering occurs at up to 65% of theoretical density. Although sample AL has a higher density than mentioned by the author, it is still in the early stage of sintering, even with an average densification above 65%. One contributing factor to pure alumina not achieving a microstructure with higher densification was the sintering temperature. Pure alumina, to obtain good densification values, should be sintered at 1600 °C, approximately 80% of its melting temperature [44].
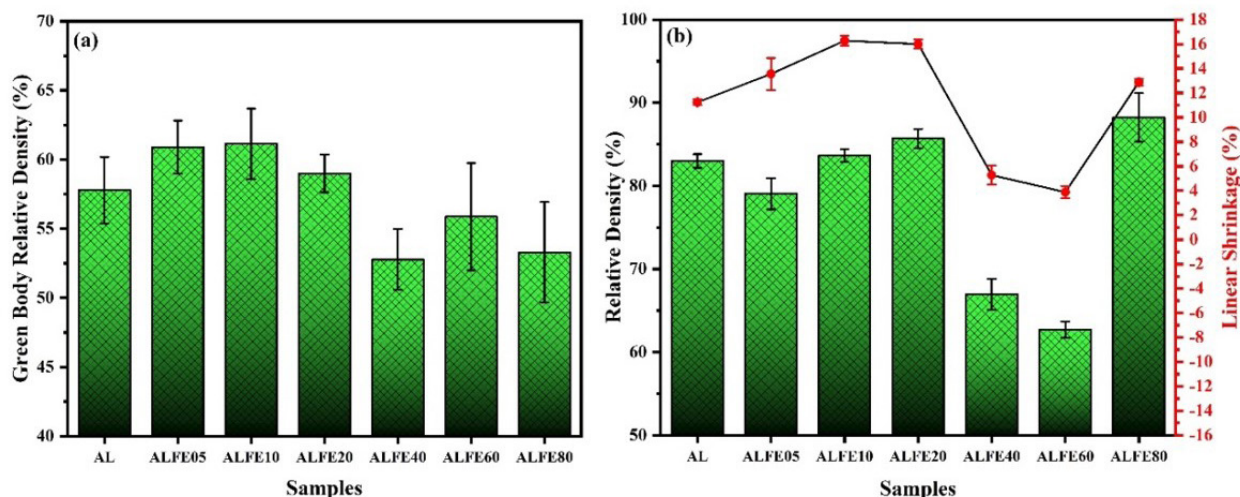
Figure 3. (a) Green body density results; (b) Relative density results of sintered samples and linear shrinkage.

The ALFE05 sample, Figure 4(b), shows a microstructure with fewer pores and larger spacings between them. Moreover, the presence of the Fe_2O_3 additive among the grains results in a greater number of grains interconnected by necks. These necks formed due to the additive's presence, promoting lower porosity in the material.

The ALFE10 sample, Figure 4(c), demonstrates that adding 1 wt.% of the additive resulted in a slight increase in grain size compared to the ALFE05 sample. This grain growth allows for a clearer visualization of neck formation during the sintering process. Like the ALFE05 sample, the ALFE10 sample exhibits characteristics of an intermediate stage of sintering, with grain growth and a microstructure full of interconnected pores. As the necks form, these pores tend to isolate [45].

On the other hand, increasing the Fe_2O_3 concentration to 2 wt.%, the ALFE20 sample shows a similar effect to the ALFE05 and ALFE10 samples, with the difference that, due to the higher average densification of these samples, there is a lower quantity and size of pores in the material. Increasing the Fe_2O_3 content to 4 and 6 wt.% resulted in an excessively porous microstructure with low density. The ALFE40 and ALFE60 samples, Figures 4(e) and 4(f), respectively, exhibit a highly porous structure. The images reveal that the sintering process was not efficient in these samples, with almost complete absence of neck formation, only a mild adhesion between grains due to diffusion during heating. This results in materials with extremely low density, implying inferior mechanical properties [46].

The ALFE80 sample, Figure 4(g), stands out from the other groups due to its remarkably dense microstructure and considerable grain growth. Additionally, it exhibits completely isolated pores, tending to assume a spherical shape. This dense microstructure with high grain growth is the result of the elevated densification values observed for the addition of 8 wt.% of Fe_2O_3, where the sample reached the final stage of sintering.
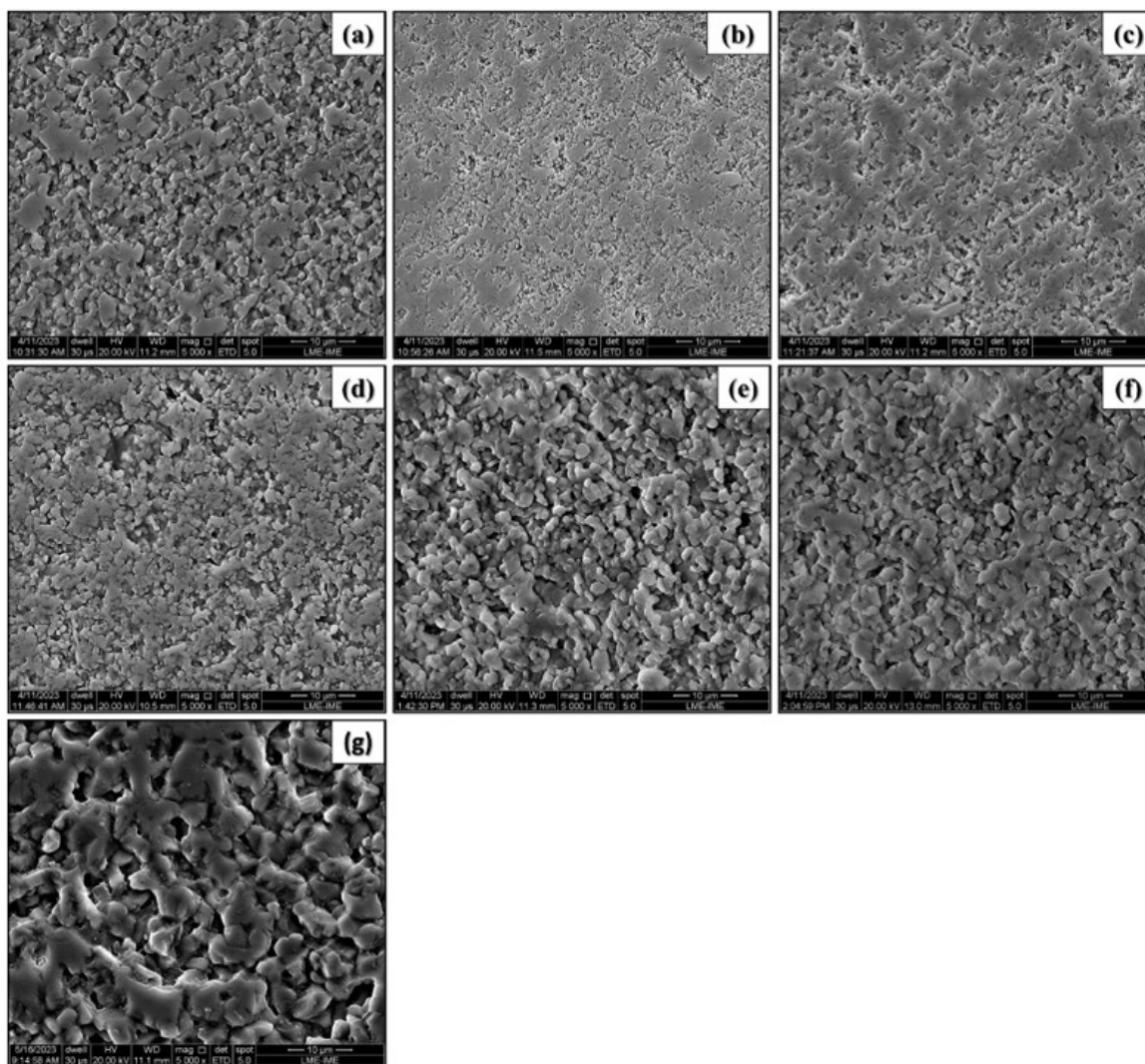

Figure 4. SEM images of the sample surfaces with a magnification of 5000x: (a) AL; (b) ALFE05; (c) ALFE10; (d) ALFE20; (e) ALFE40; (f) ALFE60; (g) ALFE80.

Figure 5 illustrates the surface images of the sintered samples and the compositional map obtained through EDS analysis. Meanwhile, Table 3 presents the weight percentages of each element present in the samples.

When analyzing the elemental mapping images, it is observed that the distribution of elements is related to the composition of oxides, and the variation in the quantity of each element occurs according to the increase in the additive content in alumina. In the AL sample, the presence of iron is not detected in its structure, as it consists solely of Al_2O_3. In the ALFE05 sample, small iron points are identified scattered throughout the sample, as can be seen in the image of overlapped elements, concentrated in regions near grain boundaries and pores. An iron content of 0.26% was found, which may be attributed to a region with a lower concentration of Fe_2O_3 in the material.
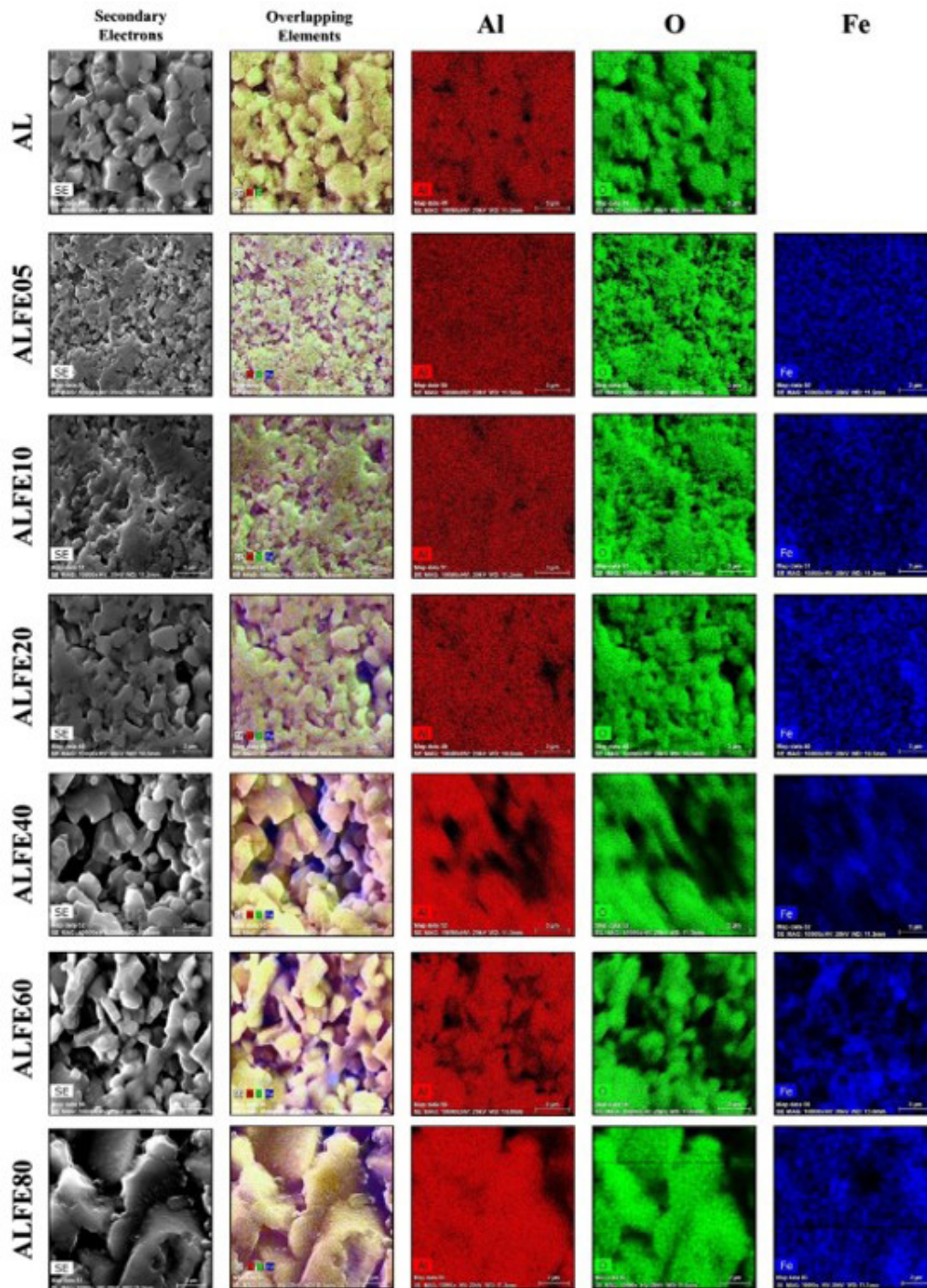
Figure 5. Compositional map of sintered samples. Magnification of 20,000x.

When analyzing samples with higher additions of Fe_2O_3, a gradual increase in the Fe content is noticeable. As the analysis progresses from the ALFE10 sample to the ALFE80 sample, concentration points of Fe are observed along the samples, indicating agglomeration of Fe_2O_3 in Al_2O_3. Despite the presence of these agglomeration zones in the ALFE05, ALFE10, ALFE20, and ALFE80 samples, the distribution of Fe in the material is quite uniform in these samples, highlighting good homogenization during the manufacturing process. However, the ALFE40 and ALFE60 samples exhibited highly agglomerated regions, especially in the porous areas of the material. The difference in density between Al_2O_3 and Fe_2O_3 (3.96 and 5.26 g/cm³, respectively) may be a likely explanation for this phenomenon. Due to its higher density, Fe_2O_3 deposited in the pores during homogenization, resulting in heterogeneous distribution, with consequent poor densification in these two samples.

Observing Table 3, it is verified that the ALFE60 sample presented a significantly lower value than 6% of Fe, exhibiting only 4.21% due to poor material homogenization, resulting in a low concentration of Fe in the analyzed region.

In addition to the compositional mapping performed on the samples, a point analysis of EDS was conducted on the sample with the highest additive content (ALFE80) to investigate the regions where Fe_2O_3 tends to deposit. Three regions were considered: the grain center, grain boundary, and grain interior. Figure 6 presents images indicating the analysis points, while the values obtained at each point are described in Table 4.

The point EDX analysis of the ALFE80 sample indicated that the sintering additive distributed itself in all grain regions, as the presence of Fe was detected at all analyzed points. However, a tendency for Fe to deposit in the grain interior was identified, where an Fe content of 8.21% was observed.
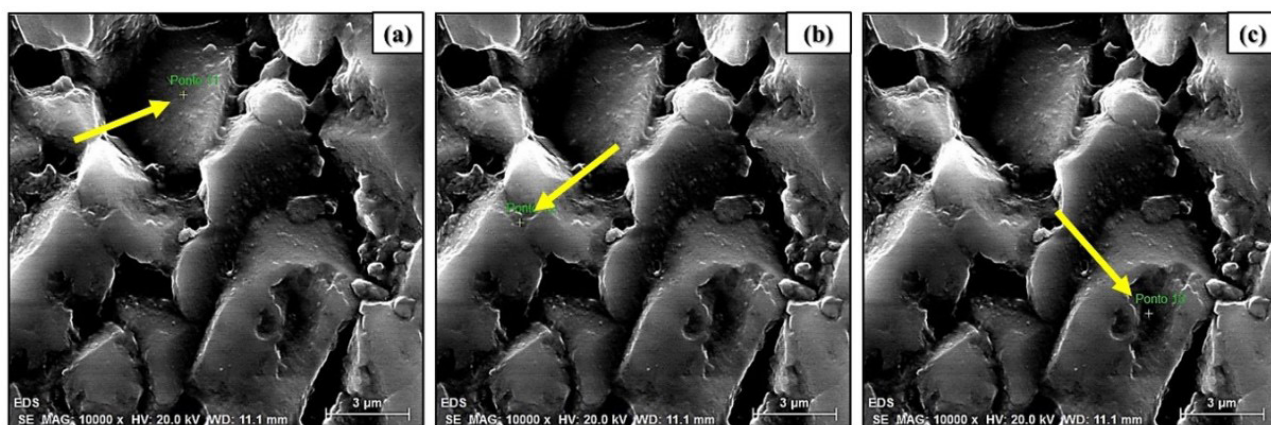
Figure 6. EDX analysis of the ALFE80 sample in different regions to determine the preferential deposition of Fe_2O_3: (a) Grain center; (b) Grain boundary; (c) Grain interior.

Table 3. Mass concentrations of the elements present in the sintered samples

SAMPLE	Al (%)	O (%)	Fe (%)
AL	57.33	42.67	-
ALFE05	56.29	43.45	0.26
ALFE10	55.91	43.31	0.78
ALFE20	57.22	41.30	1.48
ALFE40	54.98	41.07	3.94
ALFE60	55.25	40.54	4.21
ALFE80	53.48	39.42	7.10

Table 4. Variation of iron content in different regions of the grain present in the EDX analysis of ALFE80 sample

Region	Al (%)	O (%)	Fe (%)
Grain Center	52.58	41.54	5.88
Grain Boundary	53.53	39.83	6.64
Grain Interior	53.65	38.14	8.21

The analysis conducted at the grain boundary revealed an Fe value of 6.64%, while at the grain center, a value of 5.88% was recorded. This indicates that, in contrast to other sintering additives, such as Nb_2O_5, which typically accumulate preferentially at grain boundaries, as reported by Gomes et al. [47], Fe_2O_3 tends to deposit in the grain interior.
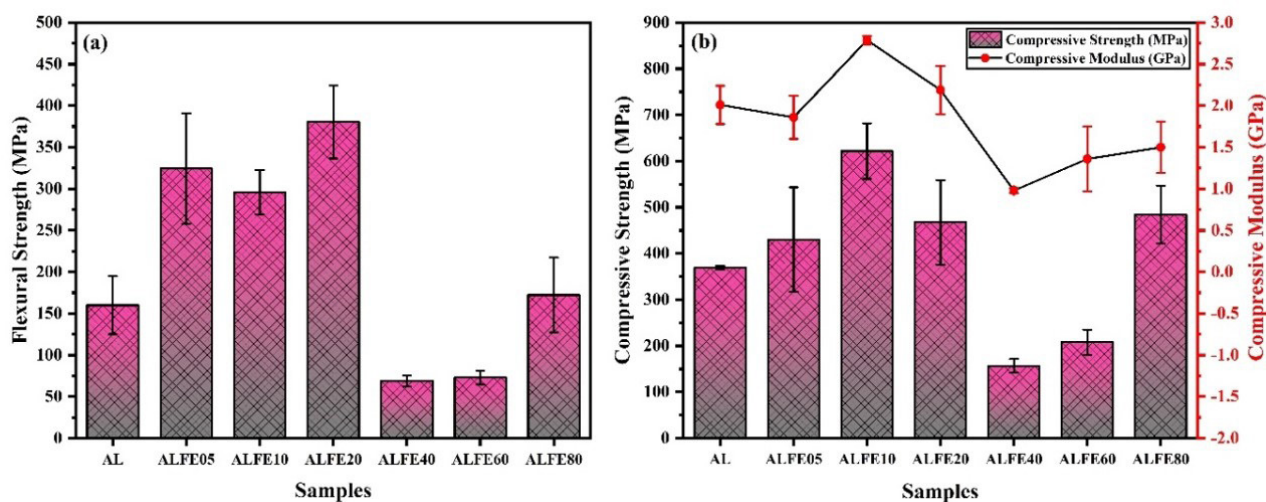
3.4 Mechanical properties

The Figure 7 presents the results of the bending and compression tests of analyzed samples.

From the results presented in Figure 7(a), it is possible to observe that the flexural strength of alumina was significantly improved with the addition of Fe_2O_3 at low concentrations. The AL group exhibited a flexural strength value of 160.07 ± 34.78 MPa. With the addition of Fe_2O_3 in fractions of 0.5, 1, and 2 wt.%, there was a considerable increase in the flexural strength of ceramics, with the ALFE05, ALFE10, and ALFE20 samples exhibiting flexural strength values of 299.84 ± 73.64 MPa, 270.48 ± 37.23 MPa, and 357.67 ± 43.30 MPa, respectively. This is directly related to the higher densification values obtained for the samples with Fe_2O_3 additions up to 2 wt.%. Furthermore, as observed through SEM images, the grains are more coalescent, favoring an increase in mechanical properties. However, the low densification of the ALFE40 and ALFE60 samples contributed to the low flexural strength of these groups, even worse than the group without the presence of Fe_2O_3. The ALFE40 and ALFE60 samples exhibited flexural strength of 63.07 ± 4.28 MPa and 62.76 ± 18 MPa, respectively. This may be associated with larger grain sizes, as seen in electron microscopy, coupled with high porosity after sintering. When comparing the flexural strength results obtained in this work with the results from Wang et al. [33], where Al_2O_3-Fe_2O_3 ceramics were produced with molar fractions of 1, 3, and 5, through uniaxial pressing at 100 MPa and conventional sintering at 1550 °C, it is evident that the values obtained by the authors were lower than the values found in this work, ranging from 48 to 68 MPa. Another example is the work of Ren et al. [48], where Al_2O_3-CaO glass-ceramics were produced with additions of Fe_2O_3 ranging from 0 to 10 wt.%, resulting in a significant increase in flexural strength, ranging from 25 MPa in the sample without Fe_2O_3 to approximately 220 MPa in the sample with 10 wt.% of the oxide. This demonstrates that through the optimization of parameters, such as applied pressure and the appropriate amount of sintering additive, the mechanical properties of alumina can be considerably improved, enabling the use of these materials in structural applications, such as refractories and abrasion-resistant ceramics, or in military applications, such as armor plates and projectile tips [49].

The results of the compressive test, displayed in Figure 5(b), show that the addition of Fe_2O_3 to Al_2O_3 followed the same trend of increase and decrease in mechanical strength values, similar to the results of densification and flexural strength. The samples from group AL had an average value of 369.27 ± 4.08 MPa. The elastic modulus was 2.01 ± 0.23 GPa. The increase in compressive strength caused by Fe_2O_3 resulted in an increase in the elastic modulus. The ALFE05, ALFE10, and ALFE20 samples had average compression strength values of 430.48 ± 113.13, 621.86 ± 60.29, and 467.43 ± 91.53 MPa, representing an increase of 16.58, 68.40, and 26.58%, respectively. The elastic modulus for ALFE05, ALFE10, and ALFE20 groups was E = 1.86 ± 0.26 GPa, 2.79 ± 0.05 GPa, and 2.19 ± 0.29 GPa, respectively. For this compound, the addition of 1 wt.% Fe_2O_3 yielded the best compressive strength result. As a result, it was almost impossible to perform the test on this group of samples since the applied load approached the testing machine's capacity (100 kN), requiring careful attention to avoid damaging the machine.

Figure 7. Mechanical properties of Al_2O_3 – Fe_2O_3 sample groups: (a) Flexural strength; (b) Compressive Strength and Modulus.

Additions of 4 and 6 wt.% Fe_2O_3 significantly reduced the strength values of the ALFE40 and ALFE60 groups. These groups had average values of 156.53 ± 14.85 and 207.86 ± 27.36 MPa, representing a reduction of 57.61 and 43.71%, respectively. The low average densification obtained in these two groups made the samples very fragile and prone to fracture. The porosity present in the microstructure prevented the samples from adequately supporting and absorbing compressive loads, leading to premature failure during the test. Consequently, the elastic modulus for both groups also showed low values, with group ALFE40 presenting $E = 0.98 \pm 0.03$ GPa, while group ALFE60 presented $E = 1.36 \pm 0.39$ GPa.

The ALFE80 group had an average compression strength value of 484.34 ± 62.62 MPa, representing an increase of 31.16% compared to the control group. Among all groups of this compound, the ALFE80 group obtained the highest densification values, reaching 88.24% of the theoretical density. However, the excess sintering additive prevented an increase in the material's strength. In addition to the sintering additive content and final densification, grain size also influences compression strength. Generally, smaller grains in the material's structure promote an increase in compression strength, while the presence of larger grains does not have as much influence on improving properties.

In the literature, there are no reports exploring the influence of grain size on the compression strength of Al_2O_3. This is due to the fact that conducting compression tests for advanced and dense ceramics is costly, requiring testing machines with high load capacity. However, there are studies evaluating this phenomenon in other materials. For example, the study by Teng et al. [50] investigated the influence of particle size on grain growth and mechanical properties of Al_2O_3. The authors used Al_2O_3 with particle sizes of 39 nm and 1.5 µm and sintered them at temperatures of 1500, 1600, and 1700 °C. It was observed that Al_2O_3 sintered with micrometer-sized particles exhibited abnormal grain growth in its microstructure, reducing its mechanical strength values. With Al_2O_3, it was possible to sinter the material without the presence of additives at 1500 °C, obtaining high values of mechanical properties, even superior to materials produced with micrometer-sized grains at higher temperatures.

In addition to grain size, porosity influences the compression strength of Al_2O_3. The more porous the sample and the larger the average pore size, the lower the compression strength of Al_2O_3. Unlike dense ceramics, Al_2O_3 ceramics are used in sectors such as the biomedical field, for example, in the development of prostheses and tissue regeneration. An example is the article by Yoon et al. [51], who developed porous Al_2O_3 ceramics, where the porosity varied from 60 to 85% of the sample volume. Compression tests revealed that the higher the porosity of the ceramic body, the lower the compression strength. This behavior was also found in the work of Castillo-Villa et al. [52], where

the authors developed Al_2O_3/graphite ceramics for acoustic applications and created ceramic bodies with controlled porosity, ranging from 21 to 58% of the sample volume. The authors obtained compression strength results close to 190 MPa for samples with lower porosity, while samples with high porosity showed a strength of approximately 30 MPa.

A third relevant factor for compression strength is the particle shape. Different shapes of Al_2O_3 particles can positively or negatively influence the strength of the ceramic material, as evidenced in the study conducted by Miyake et al. [53]. In this research, the authors investigated the sintering of Al_2O_3 ceramics at different temperatures using particles in the form of rods, disks, and spheres. The results showed that samples produced at 1600 °C from disk-shaped powder had a compression strength of approximately 100 MPa. On the other hand, samples sintered at 1500 °C using rod-shaped particles reached a value close to 250 MPa. Finally, samples produced from spherical-shaped powder, sintered at 1320 °C, achieved compression strength values of approximately 850 MPa.

4 Conclusions

In this study, ceramics of the Al_2O_3 - Fe_2O_3 compound were produced with the aim of enhancing the understanding of their physical, mechanical, and microstructural properties. To achieve this goal, various analyses were conducted, such as dilatometry, density measurement, scanning electron microscopy (SEM), energy-dispersive spectroscopy (EDX), and flexural and compression tests. The obtained results led to the following conclusions:

After dilatometric analysis, it was observed that the addition of Fe_2O_3 in fractions of 1 and 2 wt.% results in an increase in linear shrinkage, while additions of 4 and 6 wt.% lead to very low shrinkage, and a slight contraction with 8 wt.%. These findings are reinforced by density analysis using the Archimedes method, which highlights the low linear shrinkage of samples with 4 and 6% of Fe_2O_3, indicating a deficiency in their densification.

SEM analyses revealed the microstructure of the sintered samples, allowing for the observation of a porous aspect in all of them. This porous aspect was reduced in the ALFE05 and ALFE10 samples but accentuated in the ALFE40 and ALFE60 samples due to their low densification, resulting in high porosity. In the ALFE80 sample, the material showed low porosity with pronounced grain growth.

EDX analyses allowed for the quantification of the elements present and their distribution in the sample. An increase in the Fe content was observed as a result of the addition of Fe_2O_3 in the samples. Furthermore, it was found that Fe was mainly located in the pores and grain boundaries of the Al_2O_3.

The results of flexural tests demonstrated a significant increase in the flexural strength of Al_2O_3 with the addition of Fe_2O_3 up to 2%. However, additions of 4% and 6% resulted in a drastic reduction in the flexural strength of

the ceramic, even worse than pure Al_2O_3. The addition of 8 wt.% of Fe_2O_3 promoted a slight increase in strength, but the marginal improvement did not justify the use of sintering additive in this quantity.

The results of compression tests demonstrated an increase in strength similar to the flexural test results; however, the ALFE10 group exhibited the highest compression strength among all groups. Similar to the density and flexural strength results, samples from the ALFE40 and ALFE60 groups presented the worst values among all groups. The addition of 8 wt.% of Fe_2O_3 increased compression strength, ranking just below the ALFE10 group.

Acknowledgements

References

1   Baltazar J, Alves MFRP, dos Santos C, Olhero S. Reactive Sintering of Al2O3–Y3Al5O12 Ceramic Composites Obtained by Direct Ink Writing. Ceramics. 2022;5(1):1-12.

2   Piconi C. Alumina. In: Ducheyne P, editor. Comprehensive biomaterials. Amsterdam: Elsevier; 2011. p. 73-94. http://dx.doi.org/10.1016/b978-0-08-055294-1.00016-7.

3   Munz D, Fett T. Ceramics: material properties, failure behavior, materials selection. Berlin: Springer; 1999.

4   Silveira P, Silva T, Ribeiro M, Rodrigues de Jesus P, Credmann P, Gomes A. A brief review of alumina, silicon carbide and boron carbide ceramic materials for ballistic applications. Academia Letters. 2021;3742:1-11.

5   Yang S, Yang S, Zhu Y, Fan L, Zhang M. Flash Sintering of dense alumina ceramic discs with high hardness. Journal of the European Ceramic Society. 2022;42(1):202-206.

6   Wu Y, Zhang Y, Choy KL, Guo J. Liquid-phase sintering of alumina with YSiAlON oxynitride glass. Materials Letters. 2003;57(22-23):3521-3525.

7   Keramat E, Hashemi B. Modelling and optimizing the liquid phase sintering of alumina/CaO–SiO2–Al2O3 ceramics using response surface methodology. Ceramics International. 2021;47(3):3159-3172.

8   German RM, Suri P, Park SJ. Liquid phase sintering. Journal of Materials Science. 2009;44:1-39.

9   Lee JW, Cha JM, Bae BH, Choi SW, Jung HD, Yoon CB. Effects of using MgO, CaO additives as sintering aid in pressureless sintering of M2Si5N8: Eu2+ (M= Ba, Sr) phosphor ceramics for amber LED automotive applications. Journal of Alloys and Compounds. 2021;858:157710.

10 Souto P, Menezes R, Kiminami R. Sintering of commercial mulite powder: Effect of MgO dopant. Journal of Materials Processing Technology. 2009;209(1):548-553.

11 Fabris DCN, Polla MB, Acordi J, Luza AL, Bernardin AM, De Noni A Jr, et al. Effect of MgO· Al2O3· SiO2 glass-ceramic as sintering aid on properties of alumina armors. Materials Science and Engineering A. 2020;781:139237.

12 Pan C, Zhao G, Li S, Wang J, Yin L, Song W, et al. Effect of BaO-2B2O3 sintering aid on the structural and electrical properties of CaBi2Nb2O9 high-temperature piezoelectric ceramic. Journal of Applied Physics. 2021;130(24):244102.

13 Silveira PHPM, Jesus PRR, Ribeiro MP, Monteiro SN, Oliveira JCS, Gomes AV. Sintering Behavior of AL2O3 Ceramics Doped with Pre-Sintered NB2O5 and LiF. Materials Science Forum. 2020;1012:190-195.

14 Gomez E, Echeberria J, Iturriza I, Castro F. Liquid phase sintering of SiC with additions of Y2O3, Al2O3 and SiO2. Journal of the European Ceramic Society. 2004;24(9):2895-2903.

15 Shan K, Li R, Liu J. Effect of Y2O3 on the corrosion resistance of two-step sintered Al5Y3O12-MgAl2O4 sidewalls in the aluminum electrolyte. Journal of the European Ceramic Society. 2022;42(4):1815-1821.

16 Carvalho ANC, Sousa Melo JJ, Sales FHS. Medidas elétricas e dielétricas em cerâmicas de BaTiO3 dopadas com SiO2 e Bi2O3. Brazilian Journal of Development. 2022;8(1):6871-6899.

17 Zaki ZI, Alotaibi SH, Alhejji BA, Mostafa NY, Amin MA, Qhatani MM. Combustion synthesis of high density ZrN/ZrSi2 composite: influence of ZrO2 addition on the microstructure and mechanical properties. Materials (Basel). 2022;15(5):1698.

18 Svancarek P, Galusek Gnanasagaran CL, Ramachandran K, Ramesh S, Ubenthiran S, Jamadon NH. Effect of co-doping manganese oxide and titania on sintering behaviour and mechanical properties of alumina. Ceramics International. 2023;49(3):5110-5118.

19 Sktani ZDI, Rejab NA, Ratnam MM, Ahmad ZA. Fabrication of tougher ZTA ceramics with sustainable high hardness through (RSM) optimisation. International Journal of Refractory Metals & Hard Materials. 2018;74:78-86.

20 Liu L, Zachariah MR. Enhanced performance of alkali metal doped Fe_2O_3 and Fe_2O_3/Al_2O_3 composites as oxygen carrier material in chemical looping combustion. Energy & Fuels. 2013;27(8):4977-4983.

21 Jiang Y, Mao Q, Ma T, Liu X, Li Y, Ren S, et al. Facile preparation of Fe_2O_3 Al_2O_3 composite with excellent adsorption properties towards Congo red. Ceramics International. 2021;47(10):13884-13894.

22 Yan P, Zhang K, Peng Y. Study of Fe_2O_3-Al_2O_3 catalyst reduction parameters and conditions for catalytic methane decomposition. Chemical Engineering Science. 2022;250:117410.

23 Hu J, Li H, Chen S, Xiang W. Enhanced Fe_2O_3/Al_2O_3 oxygen carriers for chemical looping steam reforming of methane with different Mg ratios. Industrial & Engineering Chemistry Research. 2022;61(2):1022-1031.

24 Ma Z, Liu G, Lu Y, Zhang H. Redox performance of Fe_2O/Al_2O_3 oxygen carrier calcined at different temperature in chemical looping process. Fuel. 2022;310:122381.

25 Abyzov A. Aluminum oxide and alumina ceramics (review). Part 1. Properties of Al_2O_3 and commercial production of dispersed Al_2O_3. Refractories and Industrial Ceramics. 2019;60:24-32.

26 Bercoff P, Bertorello H. Magnetic properties of hematite with large coercivity. Applied Physics. A, Materials Science & Processing. 2010;100:1019-1027.

27 Muan A, Gee C. Phase equilibrium studies in the system iron oxide-Al_2O_3 in air and at 1 Atm. O_2 pressure. Journal of the American Ceramic Society. 1956;39:207-214.

28 Muan A. On the stability of the phase Fe_2O_3. Al_2O_3. American Journal of Science. 1958;256:413-422.

29 Dayal R, Gard J, Glasser F. Crystal data on $FeAlO_3$. Acta Crystallographica. 1965;18:574-575.

30 Feenstra A, Sämann S, Wunder B. An experimental study of Fe–Al solubility in the system corundum–hematite up to 40 kbar and 1300 C. Journal of Petrology. 2005;46(9):1881-1892.

31 Dreval L, Zienert T, Fabrichnaya O. Calculated phase diagrams and thermodynamic properties of the Al_2O_3–Fe_2O_3–FeO system. Journal of Alloys and Compounds. 2016;657:192-214.

32 Majzlan J, Navrotsky A, Evans B. Thermodynamics and crystal chemistry of the hematite–corundum solid solution and the $FeAlO_3$ phase. Physics and Chemistry of Minerals. 2002;29:515-526.

33 Wang ZF, Wang JS, Chen YJ, Yu LX, Bu JL, Wang RL. Effect of molar ratio of Al_2O_3 to Fe_2O_3 on the sintering and thermal shock resistance of Al_2O_3-Fe_2O_3 composite. Advanced Materials Research. 2011;194:1745-1748.

34 Cao Z, Qin M, Jia B, Gu Y, Chen P, Volinsky AA, et al. One pot solution combustion synthesis of highly mesoporous hematite for photocatalysis. Ceramics International. 2015;41(2):2806-2812.

35 Maca K, Pouchly V, Boccaccini A. Sintering densification curve: a practical approach for its construction from dilatometric shrinkage data. Science of Sintering. 2008;40(2):117-122.

36 Associação Brasileira de Normas Técnicas. NBR 16661:2017: Material refratário denso conformado – determinação de volume aparente, volume aparente da parte sólida, densidade da massa aparente, densidade aparente da parte sólida, porosidade aparente e absorção. 2. ed. Rio de Janeiro: ABNT; 2017.

37 Associação Brasileira de Normas Técnicas. NBR ISO 6872: Odontologia – Materiais Cerâmicos. Rio de Janeiro: ABNT; 2023.

38 Awaju H, Watanabe T, Nagano Y. Compressive testing of ceramics. Ceramics International. 1994;20(3):159-167.

39 Pouchly V, Maca K. Master sintering curve: a practical approach to its construction. Science of Sintering. 2010;42(1):25-32.

40 Ribeiro GC, Fortes BA, Silva L, Castro JÁ, Ribeiro S. Evaluation of mechanical properties of porous alumina ceramics obtained using rice husk as a porogenic agent. Cerâmica. 2019;65(1):70-74. http://dx.doi.org/10.1590/0366-6913201965s12604.

41 Zygmuntowicz J, Piątek M, Miazga A, Konopka K, Kaszuwara W. Dilatrometric sintering study and characterization of alumina-nickel composites. Processing and Application of Ceramics. 2018;12(2):111-117.

42 García DE, Schicker S, Bruhn J, Janssen R, Claussen N. Processing and mechanical properties of pressureless-sintered niobium-alumina-matrix composites. Journal of the American Ceramic Society. 1998;81(2):429-432.

43 Jesus PRR, Silveira PHPM, Ribeiro MP, Silva TT, Arantes VL, Gomes AV. Fabrication of al2o3-nb2o5-lif-zro2 fgms by sps method: microstructural evaluation, dynamic and sintering behaviour. Processing and Application of Ceramics. 2022;16(3):251-258.

44 Taktak R, Baklouti S, Bouaziz J. Effect of binders on microstructural and mechanical properties of sintered alumina. Materials Characterization. 2011;62(9):912-916.

45 Lakshmanan A. Sintering of ceramics: new emerging techniques. Rijeka: Books on Deman; 2012.

46 Ortega FS, Paiva AEM, Rodrigues JÁ, Pandolfelli VC. Propriedades mecânicas de espumas cerâmicas produzidas via. Cerâmica. 2003;49(309):1-5. http://dx.doi.org/10.1590/s0366-69132003000100002.

47 Gomes A, Louro L, Costa C. Ballistic behavior of alumina with niobia additions. Journal de Physique. IV. 2006;134:1009-1014.

48 Ren XZ, Zhang W, Zhang Y, Zhang PX, Liu JH. Effects of Fe2O3 content on microstructure and mechanical properties of CaO–Al2O3–SiO2 system. Transactions of Nonferrous Metals Society of China. 2015;25(1):137-145.

49 Medvedovski E. Alumina–mullite ceramics for structural applications. Ceramics International. 2006;32(4):369-375.

50 Teng X, Liu H, Huang C. Effect of al2o3 particle size on the mechanical properties of alumina-based ceramics. Materials Science and Engineering A. 2007;452:545-551.

51 Yoon BH, Choi WY, Kim HE, Kim JH, Koh YH. Aligned porous alumina ceramics with high compressive strengths for bone tissue engineering. Scripta Materialia, Elsevier. 2008;58(7):537-540.

52 Castillo-Villa PO, Baró J, Planes A, Salje EK, Sellappan P, Kriven WM, et al. Crackling noise during failure of alumina under compression: the effect of porosity. Journal of Physics Condensed Matter. 2013;25(29):292202.

53 Miyake K, Hirata Y, Shimonosono T, Sameshima S. The effect of particle shape on sintering behavior and compressive strength of porous alumina. Materials, MDPI. 2018;11(7):1137.